RBT 1.0: A 3D Multimodal MRI Stereotaxic Atlas of the Rabbit Brain

Zhanbo Zhang[1,3], Tianhao Zhou[1,3], Yong Yang[1,3], Chenfei Cao[1], Yu Zhang[1], Quetao Yu[1], Jixiang Zeng[1], Xuan Zhou[1], Xiaoming Wang[1], Ruiqi Tian[1], Xiaodong Zhang[1], Yao He[2], Feng Yue[1*], Pengcheng Li[1*], and Junjie Zhuo[1*]

1. *State Key Laboratory of Digital Medical Engineering, Key Laboratory of Biomedical Engineering of Hainan Province, School of Biomedical Engineering, Hainan University, Sanya;*
2. *Macau University of Science and Technology, Macau;*
3. *These authors contributed equally*

* *Correspondence: Address: fyuee@hainanu.edu.cn; pengchengli@hainanu.edu.cn; junjie.zhuo@hainanu.edu.cn;*

ABSTRACT

The rabbit serves as a critical bridge species in translational neuroscience due to its human-like neurodevelopmental trajectories, white matter architecture, and biophysical neuronal properties. However, the lack of a standardized, high-resolution in vivo brain atlas has significantly impeded its broader adoption in systems neuroscience and disease modeling. In this study, we established a multimodal, population-averaged in vivo template and stereotaxic framework for the adult New Zealand White rabbit by integrating 5.0 T in vivo MRI, 9.4 T ex vivo MRI, and micro-CT imaging. Using multi-contrast priors, we systematically identified 107 fine-grained regions across the cortex, white matter, and subcortical structures. To facilitate broad accessibility, we developed a deep learning-based pipeline that enables fully automated whole-brain segmentation, eliminating the need for manual preprocessing. Our results demonstrate that this atlas effectively captures native anatomical states, overcoming the tissue deformation inherent in legacy ex vivo templates. With a fully differentiated striatum and a brain volume sixfold larger than that of rodents, this framework provides a superior platform for translational brain disease research and longitudinal functional imaging. By providing a publicly available, anatomically accurate reference, this work establishes a standardized foundation for neuroscientific research across the evolutionary continuum.

Keywords: Rabbit; Atlas; Template, MRI; In vivo; Neuroimaging;

INTRODUCTION

The rabbit has been a classic model in neurological research since the nineteenth century (Sawyer et al., 1954). With the revolutionary advancement of rodent gene-editing technologies, the selection of laboratory animal models has exhibited a pronounced "rodent-centric" trend (Manger, 2008; Seyhan, 2019). Nevertheless, rabbits

Uncorrected proof

remain indispensable as non-rodent models in neuroscience research. Compared to rodents, rabbits share greater homology with humans in neurodevelopmental trajectories and white matter architecture, as rabbits are perinatal brain developers with human-like white matter maturation timing (Derrick et al., 2007; Eixarch et al., 2012). Moreover, rabbit cortical neurons exhibit biophysical features and soma sizes that are evolutionarily scaled to be more similar to humans than to smaller animals like rodents (Beaulieu-Laroche et al., 2021). These unique neuroanatomical and functional characteristics make rabbits an optimal model for studying neurological disorders such as stroke (Kim et al., 2021; Narayan et al., 2021; Seo et al., 2022; Yang et al., 2009), Parkinson's disease (Hayrapetyan and Badalyan, 2023; Leao et al., 2015), and Alzheimer's disease (Jin et al., 2018; Rozema et al., 2020; Weiss et al., 2022a). Recent progress in gene-editing technologies, particularly CRISPR/Cas9, has driven breakthroughs in rabbit model development, providing promising novel tools for brain disease research (Han et al., 2024; Zhang et al., 2022).

While electrophysiological and neuroimaging research on the rabbit brain has advanced remarkably in recent years, the field still lacks essential anatomical tools to drive further progress. As a result, researchers often rely on outdated 2D photographic references (Plum, 2004) or resort to labor-intensive manual segmentation (Brusini et al., 2018; Schroeder et al., 2016; Weiss et al., 2022b; Weiss et al., 2018). The absence of a standardized, detailed stereotaxic atlas precludes the automated, region-specific mapping and large-scale population analyses that are well established in other species (Balan et al., 2024b; Kleven et al., 2023; Mansour et al., 2025; Tian et al., 2022; Wang et al., 2020).

This gap persists despite various efforts to develop MRI-based digital atlases, as most available resources remain unsuitable for general research needs. Many rely on anisotropic resolution, which compromises spatial resolution and 3D structural continuity. For instance, an average adult rabbit template was constructed with a resolution of $0.15 \times 0.15 \times 0.7$ mm^3, where the coarse axial resolution restricted the precision of volumetric analysis (Muñoz-Moreno et al., 2013). While high-resolution isotropic imaging (0.078 mm) has been achieved at 9.4T, such efforts have been limited to neonatal specimens (Ferraris et al., 2018). Critically, the majority of existing atlases utilize ex vivo specimens, which are known to undergo significant morphological distortion compared to in vivo tissue. Critically, the majority of existing atlases utilize ex vivo specimens, which are known to undergo significant morphological distortion compared to in vivo tissues (Lee et al., 2021). Although an in vivo 3T MRI-based atlas has been developed, its coarse anisotropic resolution ($0.4 \times 0.4 \times 2.2$ mm^3) constrains analysis to coronal interpretations, and importantly, no publicly available digital version has been released to date (Mullhaupt et al., 2015).

To address these gaps, we present RBT, a comprehensive and integrated framework that encompasses a multimodal rabbit brain template, a highly detailed anatomical atlas, and a standardized stereotaxic space. By integrating cross-scale 5.0T in vivo and 9.4T ex vivo MRI with 20-μm micro-CT skull data, we established a unified coordinate system that precisely aligns neuroanatomy with stereotaxic landmarks. Leveraging this system, we provide a detailed in vivo anatomical atlas, with refined

Uncorrected Proof

spatial delineation of brain structures. Additionally, we incorporated an open-source deep learning pipeline for automated whole-brain extraction and segmentation, eliminating the need for manual intervention. As a publicly available resource, RBT provides both a standard anatomical reference and an automated processing pipeline, facilitating broader applications in rabbit-based neuroscience.

MATERIALS AND METHODS

Ethics statement

All animal experiments were performed in accordance with the Guide for the Care and Use of Laboratory Animals, and obtained approval from the Experimental Animal Ethics Committee in Hainan University (Approval number: HNUAUCC-2025-00087).

Animal selection and sample collection

Experimental Animals. Ten healthy adolescent male New Zealand White rabbits, with a mean age of 8 weeks and a mean body weight of 2.39 ± 0.16 kg, were selected for this study (Supplementary table. 1). The animals were housed in a controlled environment for a 3-day acclimation period, with a 12-hour light/dark cycle and ad libitum access to food and water.

In Vivo Image Acquisition. In vivo imaging was conducted using a 5.0T MRI scanner (uMR Jupiter, United Imaging Healthcare, Shanghai, China) equipped with a 24-channel human Tx/Rx knee coil (Fig. 1a). Anesthesia was induced by intramuscular injection of Zoletil (Virbac, France; 0.3 ml/kg) and maintained with ~1.0% isoflurane (RWD, Shenzhen, China) delivered via a ventilator following endotracheal intubation. A Vitamin E capsule was placed near the left eye to serve as an anatomical lateral marker. The rabbits were positioned prone with the head immobilized at the center of the magnetic field using a customized acrylic headframe (Supplementary Fig. 1). To determine the optimal number of signal averages (NSA) that balances image quality with acquisition time efficiency, we conducted a preliminary analysis examining the relationship between SNR and NSA. The resulting SNR-NSA curve, presented in Supplementary Fig. 2, informed the selection of NSA = 12 for both structural sequences, ensuring adequate signal quality for high-resolution template construction while maintaining clinically feasible scan durations. T1-weighted images (T1w) were performed using a fast spoiled gradient-recalled echo (FSPGR) sequence with the following parameters: TR = 14.5ms, TE = minimum, flip angle = 9°, read/phase FOV = 58/52 mm, matrix = 176 × 100, slice thickness = 0.33mm, and NSA = 12. T2-weighted images (T2w) were obtained using a 3D variable flip angle fast spin-echo (Matrix) sequence with the following parameters: TR = 3000ms, TE = 342ms, read/phase FOV = 52/52 mm, matrix = 160 × 100, slice thickness = 0.33 mm, and NSA = 12.

Ex Vivo Sample Preparation and Imaging. Following in vivo imaging, a rabbit was randomly selected for euthanasia. Pericranial soft tissues and non-bony appendages were surgically excised to preserve the integrity of skull and brain tissue. The samples were fixed in 4% paraformaldehyde solution at 4°C for 2–4 hours and subsequently transferred to 30% sucrose solution at 4°C for dehydration until they sank. Prior to imaging, specimens were immersed in Fluorinert to mitigate magnetic susceptibility

Uncorrected Proof

artifacts. Structural data were initially acquired using Micro-CT with an isotropic resolution of 72 μm (reconstruction matrix = 1024 × 1024, slice thickness = 72 μm). Subsequently, multimodal imaging was performed on a 9.4T ultra-high-field MRI scanner (uMR 9.4T, United Imaging Life Science Instrument, Wuhan, China) equipped with a Transmit-Receive Volume Coil-42. Ex vivo T2w were carried out using a 3D turbo spin-echo (TSE) sequence with a spatial resolution of $0.03 \times 0.06 \times 0.03 mm^3$ and the following parameters: TR = 3.5ms, TE = 14.24ms, read/phase FOV = 32.01/27.96 mm, matrix = 1004 × 466, and slice thickness = 0.06 mm. Quantitative susceptibility mapping (QSM) was acquired using a 3D multi-echo gradient-recalled echo (GRE) sequence with an isotropic resolution of 0.15 mm and the following parameters: TR = 50ms, number of echoes = 5, TE1/TE5 = 3/19ms, read/phase FOV = 40.03/38.40 mm, matrix = 267 × 256, and slice thickness = 0.15 mm.

To provide a comprehensive overview of the data acquisition strategy, the imaging modalities employed for each individual subject and their corresponding acquisition purposes are summarized in Supplementary Table 2.

Multimodal Image Preprocessing

Structural Image Preprocessing. Non-local means denoising (Manjon et al., 2010) was applied to the in vivo T1w and T2w structural images using the DenoiseImage module of the ANTs software package (Avants et al., 2009). Next, the N4ITK algorithm (Tustison et al., 2010) was employed for iterative bias field correction to mitigate inhomogeneities. To account for inter-subject variations in signal intensity, histogram matching was performed for intensity standardization. Finally, all MRI data were resampled to an isotropic resolution of 0.15 mm using B-spline interpolation.

QSM Reconstruction. Quantitative susceptibility maps were reconstructed from GRE sequence data using the open-source QSMxT framework (Stewart et al., 2022). Initially, rigid-body registration was applied to each echo image to align them to the first echo space. During phase preprocessing, the ROMEO algorithm was used for 3D phase unwrapping (Dymerska et al., 2021), followed by multi-echo weighted fitting to enhance the signal-to-noise ratio (SNR) of the phase maps. The average multi-echo image was calculated, and the ANTs getMask module was used to extract the largest connected component for an initial mask, which was manually refined to define the final whole-brain anatomical boundaries. This mask was then used as a spatial constraint for the variable-kernel V-SHARP algorithm to remove background magnetic field components (Wu et al., 2012). Finally, the processed local phase maps were reconstructed into quantitative susceptibility maps using the truncated k-space division (TKD) technique (Wharton et al., 2010).

CT Image Processing and Skull Extraction. For the CT images, an automatic thresholding strategy based on Otsu's method was employed to binarize the volumetric data and isolate the high-density skull bone region. The implementation was carried out using the ANTsPy library (otsu_segmentation), with the number of classes (k) set to 7. From the resulting multi-class segmentation, tissue classes 1, 2, and 3 were systematically excluded to refine the isolation of bone tissue. To ensure structural continuity, a morphological closing algorithm (radius = 2) was applied to the preliminary masks. These masks were subsequently imported into ITK-SNAP

Uncorrected Proof

(Yushkevich et al., 2006) for manual refinement. Using the 3D visualization and interactive painting tools provided by ITK-SNAP, we accurately labeled the identified skull structures and erased non-skull high-density artifacts, while filling small gaps to ensure anatomical accuracy.

Establishment of the Standard Rabbit Brain Space

Multimodal Image Fusion and Alignment. To construct the standard brain space, we implemented a rigorous multimodal registration pipeline. (1) MRI Skull Information Extraction: For the ex vivo T2w MRI, an initial brain mask was generated using the get_mask() function in ANTs, followed by manual refinement in ITK-SNAP to ensure anatomical precision. By utilizing this refined brain mask to exclude internal brain tissue signals, the surrounding skull signals were effectively isolated and identified. (2) Registration Pipeline and Similarity Metric: Prior to alignment, the high-resolution CT images were downsampled to match the spatial resolution of the ex vivo MRI. Subsequently, the aforementioned masks were applied to isolate the authentic tissue signals, and a rigid-body registration was performed on these skull-specific images that retained their grayscale information. For this multimodal alignment, Mutual Information (MI) was employed as the similarity metric. Following the automated process, a final stage of manual alignment and correction was conducted in ITK-SNAP to ensure perfect spatial correspondence between the CT and ex vivo MRI. (3) Visualization of Alignment Quality: The precise correspondence of the skull structures between the co-registered CT and ex vivo MRI images is demonstrated in the Supplemental Data (Supplementary Fig. 3).

Anatomical Landmark Identification and 3D Visualization. Three-dimensional modeling was performed on the fused images using 3D Slicer to generate a brain-skull surface model (Fedorov et al., 2012). Based on established rabbit stereotactic anatomical criteria, two key cranial landmarks were identified: Bregma (the junction of the coronal and sagittal sutures) and Lambda (the junction of the lambdoid and sagittal sutures). Simultaneously, the midpoints of the anterior commissure (AC) and posterior commissure (PC) were manually labeled within the MRI space to define the AC-PC line (Fig. 1a). This line served as the endogenous anatomical reference axis, providing a reference for aligning intracranial structures with the external coordinate system.

In vivo Registration and Landmark Mapping. To bridge the ex vivo anatomical information with the in vivo standard space, a multi-modal registration strategy was implemented. The ex vivo T2w images, following the removal of non-brain signals via refined masks, were mapped onto the in vivo template using the Symmetric Normalization (SyN) non-linear registration algorithm in ANTs, with Mutual Information (MI) as the similarity metric. Subsequently, the resulting deformation fields were utilized to project the identified landmarks (Bregma, Lambda, AC, and PC) from the ex vivo space onto the in vivo standard space. To ensure the highest mapping precision, these projected landmarks underwent rigorous manual verification and correction to guarantee perfect alignment with the corresponding anatomical features in the standard space.

Standardized Coordinate Definition and Transformation. To prioritize clinical translation and stereotaxic surgical compatibility, a dual-coordinate framework was

Uncorrected Proof

established with skull-based external references as the primary anchor. Affine transformation matrices were computed to reconstruct the standardized coordinate spaces as follows: (1) Bregma-centered System: Serving as the principal clinical coordinate system, the stereotaxic framework was constructed using Bregma as the absolute origin. The horizontal plane was defined by leveling the identified Bregma and Lambda points (flat-skull position), with the Y-axis aligned along the anatomical midline. This skull-based configuration directly interfaces with conventional surgical coordinates, enabling seamless translation between imaging and intraoperative navigation. (2) AC-PC System: As a complementary internal anatomical reference, the coordinate origin was set at the AC point. Rotational transformations were applied to align the Y-axis with the AC-PC line, ensuring that the anterior-posterior (AP) axis coincided with the endogenous reference axis. (3) Planar Constraint: The Y-Z plane was constrained to be parallel to the reference plane, aligning the reconstructed coronal, sagittal, and horizontal sections with standardized rabbit brain anatomical conventions. Both coordinate systems were integrated into the atlas via dual-scale ticks, with Bregma-based coordinates presented as the default surgical reference and AC-PC coordinates provided for cross-species neuroanatomical alignment.

Construction of the Multimodal Rabbit Brain Template

Spatial Pre-alignment and Symmetry Enhancement. The preprocessed in vivo T1w and T2w images from 10 subjects were mapped into the standard space defined by the ex vivo sample using rigid-body registration, ensuring spatial consistency across modalities and individuals. To address local registration errors resulting from contrast differences between T1w and T2w images, ITK-SNAP was employed for interactive manual refinement of images exhibiting significant spatial offsets, thereby ensuring accurate anatomical alignment. Due to limited sample size (n = 10), axial mirroring was bilaterally applied to the corrected images, generating 10 mirrored samples to augment the dataset and enhance SNR. By integrating the original and mirrored samples, a dataset of 20 images was created, improving anatomical contrast while preserving overall bilateral symmetry for template construction.

Generation of the Standardized Multimodal Template: A standardized rabbit brain template was generated through a multi-stage optimization workflow, outlined as follows: (1) Initial average reference generation: A voxel-wise arithmetic mean was calculated across all spatially pre-aligned images to create an initial population-averaged reference image; (2) Linear reference template optimization: A two-stage registration algorithm, incorporating both rigid-body and affine transformations, was applied to map individual images onto the initial reference. Through iterative averaging, a linear reference template with preliminary anatomical features was generated; (3) Non-linear deformation calculation: A symmetric normalization (SyN) algorithm (Avants et al., 2008) was used to calculate the mutual deformation fields between individual images and the linear template to generate corresponding resampled images; (4) Convergence and detail enhancement: The deformed resampled images underwent weighted averaging to update the reference template iteratively. This process was repeated to suppress random noise via population averaging, enabling the anatomical details of the template to converge and resulting in a final standard rabbit brain template

Uncorrected Proof

with a high contrast-to-noise ratio (CNR). Additionally, a version downsampled to 0.33 mm isotropic resolution is available.

Anatomical Segmentation of the Rabbit Brain

Hemispheric Mapping and Labeling. To maintain structural consistency, mirror-symmetry enhancement was incorporated during the construction of the standardized template. Anatomical delineation was initially performed in the left hemisphere; subsequently, regions of interest were mapped to the right hemisphere via mid-sagittal plane mirroring. Bilateral-specific labels were assigned according to standardized anatomical nomenclature.

Anatomical Delineation Criteria. In this study, brain regions were manually delineated within the 0.15 mm isotropic population-averaged template space. The anatomical boundaries were primarily established by synthesizing information across multiple modalities: macroscopic morphology from in vivo MRI, microscopic details from ex vivo high-resolution T2w imaging, and magnetic susceptibility contrast from QSM (Fig 1b). Boundary definition was guided by the classic histology-based rabbit brain atlas (Plum, 2004) and further refined by integrating delineation principles from the Waxholm Space rat brain atlas (Kleven et al., 2023) to ensure consistency with modern digital neuroanatomical standards. To establish definitive anatomical boundaries, the annotation process utilized 386 coronal slices as the primary axis, with concurrent reference to sagittal and horizontal planes to provide multidimensional spatial constraints. The definition of cortical regions was guided by high-resolution 2D histological sections, with morphological tracing performed along intensity gradients and sulcal landmarks to maintain the anatomical continuity of laminar structures within the 3D topological space. Boundaries for white matter systems were defined based on the distribution characteristics of histological myelin staining. These systems include the internal and external capsules, corpus callosum, cingulum, optic tract, and cerebral peduncles. MRI data were used to verify the large-scale anatomical trajectory of these fiber bundles. Cerebellar structures were partitioned into the hemispheres and vermis using the structural contrast provided by T1w imaging, with spatial validation and boundary calibration performed via serial histological sections.

Multimodal Contrast-Driven Substructural Refinement. Individual QSM were aligned to the unified template space to integrate multimodal information. The physical discrepancies between the paramagnetism of deep gray matter nuclei and the diamagnetism of white matter tracts were leveraged to define boundaries for nuclei exhibiting signal overlap in conventional structural images. Based on magnetic susceptibility contrast, subregional differences between the primary (V1) and secondary (V2) visual cortices were identified, and microstructures such as the geniculate body (GB) and anteroventral thalamic nucleus (AV) were segmented. Furthermore, the boundary information provided by QSM was utilized for the structural refinement of the striatum and periaqueductal gray (PAG), gradually completing the anatomical annotation from macroscopic structures to subregional microstructures.

Detailed Delineation Criteria. Cortical parcellation was established by delineating the cerebral cortex into frontal, temporal, parietal, piriform, medial prefrontal, cingulate, insular, and entorhinal regions, with the V1 and V2 additionally resolved through QSM

Uncorrected Proof

contrast (Supplementary Fig. 4a). Boundary definition adhered to the architectonic principles of the Plum (2004) atlas while incorporating laminar delineation standards from the Waxholm Space rat brain atlas (Kleven et al., 2023) to ensure cross-species consistency in neocortical segmentation.

Anatomical boundaries were primarily established through the synthesis of macroscopic landmarks across the anterior-posterior axis and coronal planes, validated by high-resolution ex vivo T2w imaging that resolved laminar intensity gradients. The emergence of the corpus callosum crossing the midline served as the definitive anterior-posterior demarcation between the medial prefrontal and posterior cingulate cortices, concurrently marking the anterior onset of the lateral insular cortex (Supplementary Fig. 4b). In the coronal plane, the dorsal boundary separating the medial prefrontal from the lateral frontal cortex was defined by the superior medial border of the cerebral hemisphere, with this sulcal landmark verified through intensity-based tracing on T1w sequences. The anterior limit of the lateral sagittal fissure (Fissura sagittalis lateralis) indicated the transition from the frontal to the parietal cortex and approximated the onset of the temporal cortex (Supplementary Fig. 4c), while its posterior termination denoted the anterior border of the occipital cortex; the superior margin of the claustrum, visible on both T2w and QSM contrasts, provided the segregating boundary between the parietal and temporal cortices in the coronal plane.

Ventral cortical regions were delineated using distinct cytoarchitectonic transitions visible on high-resolution histological sections. The termination of the olfactory bulb, proximal to the corona radiata, defined the anterior pole of the piriform cortex (Supplementary Fig. 4c), with this boundary further validated by the characteristic magnetic susceptibility patterns of the underlying white matter tracts on QSM. Posteriorly, the disappearance of the claustrum marked the anterior limit of the entorhinal cortex (Supplementary Fig. 4d). The rhinal fissure (Fissura rhinalis) provided a continuous lateral superior boundary for the ventral cortices, strictly separating the piriform cortex from the adjacent frontal, insular, and anterior temporal cortices; at more caudal levels, this sulcal landmark served as the distinct anatomical demarcation segregating the entorhinal cortex from the overlying temporal lobe, with these ventral boundary definitions cross-referenced against myeloarchitectonic staining patterns to ensure laminar continuity within the 3D topological space.

The hippocampal formation exhibits distinct tissue contrast across T1w, T2w, and QSM sequences, enabling direct differentiation from adjacent cortical and subcortical structures based on characteristic signal intensities and magnetic susceptibility profiles (Supplementary Fig. 5). The entorhinal cortex (EC) is delineated using the head of the hippocampus (pes hippocampi) as its dorsomedial anatomical landmark, with the EC positioned ventrolateral to the hippocampal formation. The boundary is defined at the coronal level where the hippocampal head achieves maximal prominence, with the rhinal fissure serving as the distinct sulcal demarcation separating the allocortical EC from the overlying temporal neocortex.

Striatal delineation was established by segmenting the striatum into the putamen and caudate nucleus, with these gray matter structures exhibiting distinct signal boundaries across T1w, T2w, and QSM sequences that facilitate their differentiation

Uncorrected Proof

from adjacent white matter systems (Supplementary Fig. 6). The two nuclear components are anatomically segregated by the internal capsule, a prominent myelinated fiber bundle visible as a hyperintense band on T1w and a hypointense band on T2w, with distinct magnetic susceptibility profiles on QSM. This white matter tract serves as the definitive anatomical landmark demarcating the putamen (lateral to the capsule) from the caudate nucleus (medial to the capsule), with the lateral boundary of the putamen further defined by the external capsule and claustrum, and the medial boundary of the caudate nucleus established by the lateral ventricular wall.

Thalamic delineation was established by identifying the thalamic complex medial to the internal capsule, with this prominent myelinated tract serving as the definitive lateral boundary across T1w, T2w, and QSM sequences (Supplementary Fig. 7). Specific nuclear boundaries were resolved by leveraging modality-specific brightness patterns. The Nucleus Reticularis Thalami (TRN), Geniculate Body (GB), and Nucleus Anterior Ventralis Thalami (NAVT) exhibited specific hyperintensity on QSM, enabling their precise localization within the thalamic complex. Conversely, the Nucleus Ventralis Basalis Thalami (NVBTh; referred to as NABTh), Nucleus Lateralis Thalami (NLT), and Habenular Nuclei (HbN) were demarcated by distinct contrast differences between T1w and QSM sequences, facilitating their differentiation from adjacent thalamic and epithalamic regions. These multimodal imaging signatures were validated against high-resolution histological sections to ensure accurate nuclear boundary definition within the three-dimensional reconstruction.

Midbrain delineation was established by identifying the mesencephalic complex bounded superiorly by the habenular stria and its caudal extension, and inferiorly by the superior boundary of the pons as demarcated by the cerebellar peduncles in the sagittal plane (Supplementary Fig. 8). Distinct tissue contrast across T1w, T2w, and QSM sequences facilitated differentiation of the midbrain from adjacent diencephalic and pontine structures. The periaqueductal gray (PAG) was delineated based on its prominent contrast signature across T1w, T2w, and QSM sequences, encircling the cerebral aqueduct (the narrow ventricular channel connecting the third and fourth ventricles). This nuclear region exhibited characteristic signal intensity patterns that distinguished it from surrounding tectal and tegmental structures. The superior colliculus (SC) was identified by its distinct laminar organization and high contrast visibility across T1w, T2w, and QSM sequences, positioned at the rostral aspect of the tectum. The inferior colliculus (IC) was demarcated caudal to the SC, exhibiting prominent structural definition on T1w and T2w imaging, with its caudal termination marking the transition to the pontine tegmentum. These boundaries were validated against high-resolution histological sections to ensure accurate nuclear topology within the three-dimensional reconstruction.

Deep Learning-Based Tool for Whole-Brain Segmentation

Dataset Construction. To establish the reference dataset required for the deep learning model, the SyN non-linear registration algorithm in ANTs was employed to map individual T1w images to the RBT standardized space. Utilizing the inverse deformation fields obtained from the registration, the 107 anatomical parcellations from the standard atlas were back-mapped and resampled into the original anatomical space

Uncorrected Proof

of each individual. Subsequently, morphological refinement and boundary correction were performed on the resulting initial labels to rectify topological distortions generated during the spatial transformation process. This workflow facilitated the construction of an individualized ground-truth dataset.

Deep Learning Framework and Architectural Configuration. The automated whole-brain segmentation model was developed based on the nnU-Net (Isensee et al., 2021) framework (Fig. 4a). This framework automatically configures the network architecture and data augmentation schemes according to the physical properties of the input images, such as voxel spacing and intensity distribution. The augmentation suite integrates spatial transformations, intensity perturbations, and elastic deformations to expand the anatomical diversity of the training data and improve model generalization.

Model Training Strategy and Configuration. The dataset containing 10 ground-truth labels was partitioned into training, validation, and test sets at a ratio of 6:2:2. Model training was conducted in a single-fold mode due to the small dataset size. The input image patch size was set to 128 × 96 × 128 voxels, with a batch size of 2. A composite loss function comprising Dice similarity coefficient and cross-entropy was utilized as the optimization objective. The training was performed for 1000 epochs. Model weights achieving the highest mean Dice on the validation set were selected for subsequent automated segmentation tasks.

Model Validation and Performance Evaluation. To evaluate segmentation performance, the Dice similarity coefficient (DSC) was computed between automated predictions and ground-truth annotations on both the validation and test sets, quantifying spatial overlap. The DSC for a given structure is defined as:

$$DSC = \frac{2|X \cap Y|}{|X| + |Y|}$$

Where X denotes the set of voxels in the predicted segmentation, Y denotes the set of voxels in the ground-truth annotation, and $|X|$, $|Y|$represents the cardinality (i.e., number of voxels).

Inter-hemispheric Asymmetry Analysis

To quantify the structural differences between the left and right hemispheres, we calculated the Asymmetry Index (ASI) for brain regions using the following formula:

$$ASI = \frac{|V_{left} - V_{right}|}{V_{left} + V_{right}} \times 100\%$$

Where Vleft and Vright represent the volumes of the regions of interest in the left and right hemispheres, respectively. By employing the absolute difference, this index represents the magnitude of asymmetry regardless of the direction of dominance, with higher values indicating greater inter-hemispheric disparity.

Assessment of Volumetric Variability

To evaluate the morphological consistency across subjects, the inter-subject coefficient of variation (CV) was calculated for all annotated brain regions. The CV for each structure was defined as the ratio of the standard deviation (σ) to the mean volume (μ), expressed as a percentage:

Uncorrected Proof

$$CV = \frac{\sigma}{\mu} \times 100\%$$

This metric served as an indicator of inter-individual anatomical variability, with lower CV values reflecting higher structural stability and consistency in the delineation process.

RESULTS

Stereotactic Space of the Rabbit Brain

This study established a standard stereotaxic reference space integrating the anatomical features of both the brain parenchyma and the cranium. Through multimodal image fusion, spatial alignment was achieved between the cranial surface anatomical features provided by ex vivo Micro-CT and the deep anatomical details provided by 9.4T MRI. The resulting joint 3D "brain-skull" model preserves the anatomical correspondence between external surgical landmarks and internal anatomical reference axes.

Within the RBT space, we implemented a dual-coordinate system to accommodate different research needs (Fig. 2c). First, a Bregma-centered stereotaxic system was established as the primary surgical coordinate reference, with Bregma defined as the origin and the Bregma–Lambda horizontal plane (flat-skull position) serving as the baseline. This skull-based configuration aligns with conventional stereotaxic protocols, facilitating precise translation between preoperative imaging and intraoperative navigation. Concurrently, a standardized AC–PC system was integrated as a complementary internal anatomical reference, with the center of the AC designated as the coordinate origin. Notably, an inherent parallel relationship exists between the Bregma–Lambda and AC–PC lines based on the anatomical structure of the adolescent rabbit brain. Through spatial reconstruction, the AC–PC axis was aligned with the Y-axis to form a RAS (Right-Anterior-Superior) orthogonal coordinate system, enabling standardized cross-regional neuroanatomical alignment. Both coordinate systems were co-registered within the atlas space, allowing for seamless bidirectional translation between surgical and imaging-based reference frames.

The results demonstrate that this dual-coordinate framework, presented via integrated scale ticks in the atlas, effectively bridges digital neuroimaging coordinates with traditional neurosurgical stereotaxic systems. This allows for the direct translation between internal anatomical coordinates and external surgical coordinates, providing a unified and highly practical baseline for population-level registration and high-precision individual annotation.

We additionally evaluated the imaging data quality employed for template construction by calculating the CNR and SNR, with results presented in Supplementary Fig. 9.

Multimodal Population-Averaged Template of the Rabbit Brain

We constructed the RBT multimodal template with a 0.15mm isotropic resolution (Supplementary Fig. 10). The generation of T1w and T2w population-averaged templates effectively mitigated inter-subject anatomical variability, yielding a high-

fidelity representation of the rabbit brain. These templates exhibit robust gray/white-matter contrast, precisely defining the boundaries of subcortical nuclei (e.g., the basal ganglia and thalamus) and major white-matter tracts, such as the internal capsule.

Population-level averaging significantly enhanced the CNR, unveiling microstructural details that were obscured in individual scans; notably, the hippocampus and striatum display highly distinct anatomical features within the RBT space. The multimodal framework leverages complementary contrast properties to optimize tissue representation. The T1w template provides superior gray and white matter differentiation and nuclear contrast, which are essential for delineating deep structures such as the geniculate body, whereas the T2w template offers heightened sensitivity to the boundaries between the brain parenchyma and cerebrospinal fluid (CSF). Accurate spatial alignment ensures voxel-wise correspondence across modalities (Supplementary Fig. 10c). Consequently, this template establishes a standardized morphological reference for automated whole-brain segmentation and a unified baseline for population-level statistical inference.

Multi-modal Atlas and Hierarchical Neuroanatomical Organization

The RBT atlas exhibits a well-defined 3D topological architecture, where cortical parcellations demonstrate high spatial continuity upon 3D reconstruction. This approach effectively visualizes the anatomical extent and boundaries of functional subregions across the brain surface (Fig. 2a). Based on the anatomical parcellations, we established a hierarchical neuroanatomical organization to systematically categorize the 107 brain regions (Fig. 2b; Supplementary table 3). This framework organizes the whole-brain structure into a multi-level tree-like architecture: gray matter components are categorized by developmental origin into the cerebral cortex, cerebral nuclei, diencephalon, and hindbrain, while white matter components are classified into projection, association, and commissural fibers.

Validation through orthogonal sections confirms that the anatomical boundaries delineated in the atlas are highly congruent with the structural features of the high-resolution population template. In the in vivo T1w template, the superior gray/white-matter contrast facilitates precise voxel-wise mapping between anatomical morphology and the superimposed color-coded labels (Fig. 2d). Furthermore, the atlas integratively displays the dual-coordinate system via scale ticks on these sections. This visual integration of AC-PC and Bregma-centered frameworks ensures that each anatomical boundary is coupled with both its internal neuroimaging coordinates and its external surgical stereotaxic coordinates. To provide comprehensive anatomical coverage, an extended set of sections with detailed dual-coordinate information is presented in the (Supplementary Fig. 11).

Spatial Distribution of Subcortical Nuclei

The 3D reconstruction of subcortical nuclei effectively visualizes the intricate anatomical details and spatial distribution of deep structures (Fig. 3a). The anterior view illustrates the morphology and relative positions of the habenular nuclei, caudate nucleus, claustrum, and septum. The lateral view systematically reveals the axial distribution of subcortical nuclei and provides a refined dissection of the thalamic

Uncorrected Proof

complex, specifically partitioned into six anatomical subregions: the thalamus (Thal-U), nucleus anterior ventralis thalami (NAVT), nucleus reticularis thalami (NRT), nucleus lateralis thalami (NLT), nucleus ventralis basalis thalami (NVBTh), and GB. Furthermore, the model unveils deeper nuclear structures, including the globus pallidus, mammillary body, and hypothalamus.

Integrated multimodal analysis confirms that these subcortical nuclei maintain clear anatomical morphology across coronal and horizontal planes (Fig. 3b, c). Notably, in QSM, the heightened sensitivity to paramagnetic substances (e.g., iron deposition) and myelin content significantly enhances the boundary contrast of gray matter nuclei, such as the thalamus and striatum. This multimodal validation reinforces the anatomical fidelity of the atlas at the voxel level (Fig. 3d). By establishing high-precision spatial correspondence, the RBT atlas provides a robust morphological reference for precise stereotaxic surgery and anatomical localization of subcortical structures.

Evaluation of Deep Learning-Based Automated Segmentation

This study implemented the fully automated extraction of 107 anatomical parcellations from the RBT rabbit brain atlas utilizing the nnU-Net deep learning framework. Qualitative evaluation results indicate that the segmentation boundaries of three randomly selected individual samples across coronal and horizontal planes exhibit high anatomical consistency with the standardized template (Fig. 4b). The 3D reconstruction results further confirm that the spatial coordinates and topological relationships of the brain regions generated by the automated segmentation possess high stability across different individuals, accurately restoring the complex anatomical and geometric features of the whole brain (Fig. 4c).

Quantitative validation revealed that the automated segmentation pipeline closely matched the semi-automated manual reference: across 59 anatomical structures, the Dice similarity coefficient (DSC) monotonically increased from small subcortical nuclei to extended cortical territories, yielding a whole-brain mean of 0.947 ± 0.002 (Fig. 4d; Supplementary Table 4). Core limbic and diencephalic regions, including the hippocampus (0.969 ± 0.002), thalamus (0.972 ± 0.001), hypothalamus (0.969 ± 0.002), periaqueductal grey (0.959 ± 0.004), and inferior colliculus (0.960 ± 0.003), all exceeded a Dice similarity coefficient of 0.95, indicating near-perfect overlap. Subcortical and cerebellar structures, including the putamen (0.930 ± 0.008), caudate nucleus (0.959 ± 0.004) , amygdala (0.946 ± 0.005), superior colliculus (0.932 ± 0.003) and cerebellar hemispheres (0.945 ± 0.004), remained well above the 0.9 reliability threshold, demonstrating robust performance even for morphologically complex nuclei. Notwithstanding, a small subset of compact subcortical structures, including the anterior commissure (AC: 0.878 ± 0.022), pontine nuclei (0.875 ± 0.033), and claustrum (0.898 ± 0.022), exhibited DSC values marginally below 0.9, which nonetheless represent acceptable segmentation accuracy given their diminutive size and inherently challenging anatomical boundaries. This hierarchical consistency confirms sub-millimeter anatomical fidelity across spatial scales and provides a high-throughput, reproducible tool for large-scale standardized rabbit neuroimaging.

To quantitatively validate the spatial localization accuracy, we assessed the Target Registration Error (TRE) across five independent in vivo subjects acquired at 0.33 mm

Uncorrected Proof

isotropic resolution. Four representative intracranial fiducial markers were strategically selected: the bilateral hippocampi and caudate nuclei. These anatomical landmarks were manually annotated in individual subject space using 3D Slicer software, and three-dimensional Euclidean distances were calculated between these manual annotations and the corresponding spatial coordinates derived from atlas mapping. The results demonstrated that the maximum TRE did not exceed 0.6 mm (Supplementary Fig. 12). Given the inherent voxel resolution of 0.33 mm, this submillimeter deviation across subjects mathematically confirms the exceptional spatial localization precision of the present atlas.

Quantitative Volumetry, Bilateral Asymmetry, and Regional QSM Analysis

Population-level volumetric analysis of the RBT atlas revealed stereotypical clustering across 107 parcels when bilateral volumes were log-transformed (Fig. 5; Supplementary Table 5). Core neuroanatomical structures clustered within narrow, non-overlapping ranges: hippocampus 280 ± 9 mm^3, frontal cortex 315 ± 6 mm^3, caudate nucleus 44 ± 2 mm^3, putamen 38 ± 1 mm^3, corpus callosum 58 ± 2 mm^3, and internal capsule 78 ± 2 mm^3. The coefficient of variation for these structures remained <5 %, confirming high inter-subject morphological consistency within the standardized rabbit brain framework. This clustering reflects a high degree of inter-subject morphological stereotypy within the rabbit brain when analyzed under a standardized spatial framework.

Analysis of ASI across key anatomical parcellations revealed distinct lateralization patterns (Supplementary Table 6). Several structures exhibited pronounced bilateral symmetry; specifically, the caudate nucleus, hippocampus, and globus pallidus yielded median ASI values of 0.146%, 0.215%, and 0.366%, respectively. Despite their intricate geometries, the primary and secondary visual cortices (V1 and V2) similarly maintained low median ASI values (0.606% and 1.006%), indicating a high degree of bilateral morphological conservation. In contrast, deep subcortical structures, such as the hypothalamus and mammillary body, displayed elevated median ASI values (3.734% and 4.221%, respectively). This suggests greater inter-hemispheric variability, likely attributable to the intrinsic morphological complexity and high surface-to-volume ratios of these small ventral structures, which accentuate subtle biological asymmetries.

Furthermore, neuroanatomical observations confirmed that the rabbit caudate nucleus and putamen are distinctly partitioned by the internal capsule. This organizational feature diverges from the fused neostriatum observed in rodents and more closely recapitulates the striatal parcellation patterns found in higher primates. Quantitative analysis corroborated this structural consistency: the internal capsule, along with the segmented caudate and putamen, exhibited remarkably low inter-subject CV (6.21%, 6.56%, and 5.94%, respectively). Additionally, all three structures demonstrated pronounced bilateral symmetry, with median ASI values of 0.146% (caudate nucleus), 0.430% (putamen), and 0.296% (internal capsule) (Supplementary Table 7). Such robust population-level stereotypic stability accurately captures the unique morphological signatures of the rabbit brain, thereby validating the anatomical precision of the RBT atlas and establishing a standardized baseline for future

Uncorrected Proof

morphometric investigations.

The anatomical atlas was subsequently registered to the QSM template to enable regional magnetic susceptibility analysis. Mean QSM values were extracted for each delineated brain region and are presented in Supplementary Fig. 13.

DISCUSSION

This study presents the first high-resolution, multimodal in vivo brain atlas of the adult New Zealand White rabbit, bridging a critical gap in existing neuroanatomical resources. By integrating 5.0 T in vivo MRI, 9.4 T ex vivo MRI, and micro-CT, we defined a unified stereotaxic coordinate framework that enables precise alignment of neuroanatomical structures with reliable spatial landmarks. Within this framework, a population-averaged template was generated at 0.15 mm isotropic resolution. Leveraging multi-contrast MRI (T1w, T2w, and QSM) alongside histology, we systematically delineated 107 fine-grained subregions across the cortex, white matter, deep gray matter, and brainstem. To facilitate broad accessibility and practical application, we further developed an end-to-end automated brain segmentation tool based on the nnU-Net framework, enabling fully autonomous whole-brain segmentation and eliminating the need for manual preprocessing.

Compared to previous MRI-based rabbit atlases, our work achieves the highest isotropic resolution (0.15 mm) and the most comprehensive parcellation (107 subregions) to date (Supplementary Table 8). Historically, the absence of high-precision digital references has forced neurophysiological studies to rely on empirical localization based on cranial landmarks, a method prone to spatial inaccuracies and limited reproducibility (Marbacher et al., 2011). The widely used adult rabbit brain atlas, constructed from ex vivo data obtained at 7.0 T MRI and delineating 60 subregions, was limited by anisotropic resolution and, crucially, is no longer publicly accessible (Muñoz-Moreno et al., 2013). Subsequently, Ferraris et al. developed a neonatal ex vivo rabbit brain template using 9.4 T MRI, which included 51 subregions but remains unsuitable for adult models due to substantial developmental morphological differences (Ferraris et al., 2018). Consequently, existing classic rabbit brain MRI atlases are derived from ex vivo brains, which are subject to fixation-induced deformation, inevitably leading to anatomical discrepancies from the native in vivo state. Beyond geometric distortions (approximately 6–7% regional linear shrinkage following perfusion-fixation) (Lee et al., 2021), formalin fixation substantially alters tissue contrast by modifying water-macromolecule interactions, resulting in significant deviations of T1/T2 relaxation times from their native physiological values (Weiskopf et al., 2021). Our work effectively addresses these cumulative limitations, including ex vivo artifacts, anisotropic resolution, and developmental-specific constraints, thereby establishing a standardized foundation for rabbit neuroimaging.

To evaluate the spatial resolution of our RBT atlas relative to other species, we compiled the in vivo templates previously published for comparison (Supplementary Table 9). While our resolution is numerically surpassed by ultra-high-field rodent imaging, where small-bore 7 T, 9.4 T, or 11.7 T systems achieve isotropic voxels down to 0.06 mm (Barriere et al., 2019; Goerzen et al., 2020; Hikishima et al., 2017; Ma et

Uncorrected Proof

al., 2008; Mackenzie-Graham et al., 2007; Martinez-Tazo et al., 2024; Nie et al., 2019; Prior et al., 2021; Ren et al., 2021; Sajja et al., 2016; Yang et al., 2022), these species possess lissencephalic brains with limited translational applicability to human gyrencephalic anatomy. Among small animal models, the common marmoset warrants special consideration as it possesses a gyrencephalic brain with cortical folding patterns comparable to humans, and notably, has been extensively characterized through ultra-high resolution imaging atlases achieving 64–80 μm isotropic resolution ex vivo (Liu et al., 2018; Liu et al., 2021; Zhu et al., 2023). Meanwhile, larger animals such as dogs and macaques are often restricted to 0.4 − 0.5 mm due to the bore diameter constraints of standard preclinical coils (Balan et al., 2024a; Jung et al., 2021; Lv et al., 2021; Nitzsche et al., 2019; Nitzsche et al., 2015; Ouyang et al., 2022). Rabbits present a unique challenge because their cranial dimensions are too large for rodent-optimized small-bore scanners yet too small to fully capitalize on the signal-to-noise ratio benefits of clinical whole-body systems. To overcome these constraints and achieve a high-definition population template, we optimized data acquisition by quantitatively balancing SNR against scan time and employed a custom-designed, MRI-compatible head-fixation device to suppress motion artifacts.

The resulting anatomical definition, characterized by distinct boundaries and superior contrast, further benefited from rigorous spatial alignment and multimodal integration. Specifically, we integrated micro-CT cranial landmarks with ultra-high-resolution 9.4 T ex vivo MRI to establish a precise stereotaxic reference in the standard bregma-lambda coordinate system (Feng et al., 2025; Mansour et al., 2025). Subregional delineation was further enhanced by QSM contrast, which capitalizes on regional variations in magnetic susceptibility to differentiate deep nuclei and sensory cortical boundaries that are often ambiguous on standard T1w or T2w images (Marques et al., 2017; Yoshida et al., 2021). Finally, by developing an nnU-Net model (Isensee et al., 2021) that generates segmentations directly from individual T1w images, we bypassed the complexities of cross-modal registration, significantly improving processing efficiency and reproducibility. This integrated approach ensures high anatomical fidelity and accurate spatial orientation while remaining reproducible across laboratories without requiring specialized or costly proprietary hardware.

The RBT atlas provides a robust analytical framework for stereotaxic targeting, neuroimaging, and brain–machine interface research. Previous rabbit neuroscience research has relied on empirical localization due to the lack of a high-precision, standardized in vivo atlas. In particular, most electrophysiological studies continue to depend on manual target estimation, which is time-consuming and prone to substantial spatial errors (Bereshpolova et al., 2007; Marbacher et al., 2011; Zhuang et al., 2013). Furthermore, earlier ex vivo rabbit templates suffer from coarse and anisotropic voxel dimensions (Muñoz-Moreno et al., 2013), which limit the accuracy of both functional localization and morphometric analysis and preclude the detection of fine-grained activation patterns in neuroimaging studies (Bertolino et al., 2021; Brusini et al., 2018; Schroeder et al., 2016; Weiss et al., 2022b; Weiss et al., 2018). Even emerging techniques such as dynamic electrode navigation still require high-resolution in vivo reference atlases to achieve reproducible spatial targeting (Xie et al., 2025). In summary,

Uncorrected proof

our RBT atlas overcomes the historical reliance on subjective expertise by providing a publicly available, anatomically accurate reference framework specifically optimized for live-animal neuroscience.

Although rodents dominate neuroscience due to well-established genetic tools and standardized atlases, their evolutionary distance from humans, characterized by simplified cortical architecture and low white matter content, limits their translational relevance for higher cognitive functions and disorders related to the basal ganglia. (Bassan et al., 2000). In contrast, rabbits exhibit neuronal biophysical properties that follow mammalian allometric scaling laws, providing a quantitative bridge between small and large mammals (Beaulieu-Laroche et al., 2021). As a non-rodent species, the rabbit possesses distinctive neuroanatomical traits: substantial white matter content, intermediate cortical gyrification, and a fully differentiated striatum (Fig. 6). Notably, the rabbit brain is approximately six times larger in volume than that of the rat, with gray and white matter volumes reaching sevenfold and eightfold greater, respectively. These features make it a highly suitable model for translational research on striatal disorders such as Parkinson's disease (Hayrapetyan and Badalyan, 2023; Leao et al., 2015) and Alzheimer's disease (Jin et al., 2018; Rozema et al., 2020; Weiss et al., 2022a). However, it is important to acknowledge the limitations of the rabbit model. Unlike gyrencephalic species such as sheep, pigs, or primates, the rabbit possesses a lissencephalic (smooth) cortex. This anatomical feature restricts its utility for research focused on cortical folding, complex gyrification-related disorders, or specific laminar organizations found in highly folded human cortices. In these specific contexts, gyrencephalic models like sheep may offer superior translational advantages.

Beyond anatomy, the rabbit offers practical advantages in awake experimental paradigms, particularly for functional MRI and electrophysiology. First, head fixation requires only a single miniature titanium skull bolt, and animals can be habituated in a single session for fully awake imaging. Second, preparation time is substantially shorter than the 4–8 days typically required for mice or 8–10 days for rats, and avoids the use of anesthesia, which may unpredictably alter functional network connectivity (Weiss et al., 2018). Third, the rabbit's natural calmness and tolerance to restraint enhance its suitability for longitudinal neuroimaging and electrophysiological recordings. While larger species like sheep are excellent for cortical studies, the technical challenges of maintaining them in a fully awake, head-fixed state for high-resolution imaging are significantly greater. Together, these attributes not only streamline experimental workflows but also position the rabbit as a more translationally relevant model for tracking neurodegenerative disease progression over time.

Several limitations of the current study warrant consideration. First, our cohort included only adolescent male rabbits within a narrow age range, thus precluding an assessment of sexual dimorphism or developmental variability. Prior literature has demonstrated significant sexual dimorphism in rabbit brain morphology, and intracranial volume is known to increase linearly with age (Bisenius et al., 2006; Cooper et al., 1999; Cooper et al., 2006). To address this, future work will expand the cohort to include both sexes across the full developmental trajectory, enabling the construction of an age- and sex-balanced dynamic template that mitigates systematic biological

UNCORRECTED PROOF

biases. Second, while the 5.0 T clinical system balanced accessibility and image quality, future studies will explore the development of custom-designed radiofrequency (RF) coils optimized for the rabbit head. Additionally, our current delineation lacks high-resolution ex vivo MRI and histological validation, which limits our ability to subdivide fine structures such as hippocampal subfields. We plan to incorporate Nissl and tyrosine hydroxylase staining as histological gold standards to refine subregional boundaries and achieve superior segmentation accuracy. Third, the deep learning segmentation model was trained and validated using anatomical labels derived from the same cohort of 10 subjects. While we employed cross-validation strategies to mitigate overfitting, this limited sample size and shared anatomical characteristics across the homogeneous cohort may result in performance metrics that represent an optimistic upper bound rather than true generalizable accuracy. To address this critical limitation and enhance model robustness, we intend to retrain the nnU-Net framework using a larger, multi-site dataset spanning multiple field strengths and diverse genetic backgrounds, which will provide independent external validation and confirm the framework's generalizability.

Data Availability

The RBT-v1.0 rabbit brain atlas—including the in vivo population-averaged template, the detailed anatomical atlas, and the deep learning–based parcellation tool—is openly available under an open-source license at both the ScienceDB repository (https://cstr.cn/31253.11.sciencedb.35665) and GitHub (https://github.com/HNU-BIE/RBT-v1.0). All neuroimaging data, templates, and multi-label maps are organized following the Brain Imaging Data Structure format (Gorgolewski et al., 2016), the gold standard for MRI-based open data, ensuring seamless integration with standard neuroimaging processing pipelines. To facilitate rapid exploration without downloading large files, an interactive online atlas viewer is available at https://hnu-bie.github.io/, enabling real-time visualization of the 2D orthogonal slices with annotated brain regions directly in web browsers.

COMPETING INTERESTS

The authors declare that they have no competing interests.

AUTHORS' CONTRIBUTIONS

J.J.Z., P.C.L., and F.Y. conceived and designed the study. J.J.Z., X.D.Z., Z.B.Z., and T.H.Z. designed the MRI experimental workflows and scanning procedures. Z.B.Z., T.H.Z., and Y.Y. performed the 5.0 T in vivo MRI, 9.4 T ex vivo MRI, and micro-CT scans. Y.Y. designed and engineered the custom stereotaxic apparatus. C.F.C. was responsible for animal husbandry and monitoring the anesthesia status during in vivo MRI scanning. Y.Z., Q.T.Y., J.X.Z., and X.Z. performed the ex vivo tissue preparation. Z.B.Z. and T.H.Z. manually segmented the 107 brain regions, constructed the population-averaged template, and developed the deep learning-based automated segmentation pipeline. X.M.W. and R.Q.T. organized the neuroimaging database and performed the stereotaxic coordinate alignment. J.J.Z., X.D.Z., and F.Y. verified the

Uncorrected proof

anatomical accuracy of the parcellation. Z.B.Z., T.H.Z., and J.J.Z. created the figures and wrote the manuscript. Y.H., P.C.L., and F.Y. assisted in manuscript revision and provided critical feedback. All authors read and approved the final version of the manuscript.

ACKNOWLEDGMENTS

This work was partially supported by the National Natural Science Foundation of China (Nos. 82260227 and 62527820); the National Key R&D Program of China (No. 2022YEF0203200); the Open Research Fund of State Key Laboratory of Digital Medical Engineering, Hainan University (No. DME20251002); Hainan University Research Start-up Fund (KYQD(ZR)20072 and KYQD(ZR)22074); the PhD Scientific Research and Innovation Foundation of The Education Department of Hainan Province Joint Project of Sanya Yazhou Bay Science and Technology City (HSPHDSRF-2024-08-010); the STI2030-Major Projects (2021ZD0200900).

The MRI experiments were conducted at the MRI center of Hainan University School of Biomedical engineering. The authors used the Deepseek and Chartgpt AI model for manuscript polishing; the authors maintain full responsibility for the accuracy of the final content.

REFERENCES

Avants BB, Epstein CL, Grossman M, et al. 2008. Symmetric diffeomorphic image registration with cross-correlation: evaluating automated labeling of elderly and neurodegenerative brain. *Med Image Anal*, **12**(1): 26-41.

Avants BB, Tustison NJ, Johnson HJ. 2009. Advanced Normalization Tools (ANTS). *Insight J*: 1-35.

Balan PF, Zhu Q, Li X, et al. 2024a. MEBRAINS 1.0: A new population-based macaque atlas. *Imaging Neurosci (Camb)*, **2**: 1-26.

Balan PF, Zhu Q, Li X, et al. 2024b. MEBRAINS 1.0: A new population-based macaque atlas. *Imaging Neuroscience*, **2**: 1-26.

Barriere DA, Magalhaes R, Novais A, et al. 2019. The SIGMA rat brain templates and atlases for multimodal MRI data analysis and visualization. *Nat Commun*, **10**(1): 5699.

Bassan H, Trejo LL, Kariv N, et al. 2000. Experimental intrauterine growth retardation alters

Uncorrected proof

renal development. *Pediatr Nephrol*, **15**(3-4): 192-195.

Beaulieu-Laroche L, Brown NJ, Hansen M, et al. 2021. Allometric rules for mammalian cortical layer 5 neuron biophysics. *Nature*, **600**(7888): 274-278.

Bereshpolova Y, Amitai Y, Gusev AG, et al. 2007. Dendritic backpropagation and the state of the awake neocortex. *J Neurosci*, **27**(35): 9392-9399.

Bertolino N, Procissi D, Disterhoft JF, et al. 2021. Detection of memory- and learning-related brain connectivity changes following trace eyeblink-conditioning using resting-state functional magnetic resonance imaging in the awake rabbit. *J Comp Neurol*, **529**(7): 1597-1606.

Bisenius ES, Veeramachaneni DN, Sammonds GE, et al. 2006. Sex differences and the development of the rabbit brain: effects of vinclozolin. *Biol Reprod*, **75**(3): 469-476.

Brusini I, Carneiro M, Wang C, et al. 2018. Changes in brain architecture are consistent with altered fear processing in domestic rabbits. *Proc Natl Acad Sci U S A*, **115**(28): 7380-7385.

Cooper GM, Mooney MP, Burrows AM, et al. 1999. Brain growth rates in craniosynostotic rabbits. *Cleft Palate Craniofac J*, **36**(4): 314-321.

Cooper GM, Singhal VK, Barbano T, et al. 2006. Intracranial volume changes in craniosynostotic rabbits: effects of age and surgical correction. *Plast Reconstr Surg*, **117**(6): 1886-1890.

Derrick M, Drobyshevsky A, Ji X, et al. 2007. A model of cerebral palsy from fetal hypoxia-ischemia. *Stroke*, **38**(2 Suppl): 731-735.

Dymerska B, Eckstein K, Bachrata B, et al. 2021. Phase unwrapping with a rapid opensource minimum spanning tree algorithm (ROMEO). *Magn Reson Med*, **85**(4): 2294-2308.

Eixarch E, Batalle D, Illa M, et al. 2012. Neonatal neurobehavior and diffusion MRI changes in

Uncorrected proof

826 brain reorganization due to intrauterine growth restriction in a rabbit model. *PLOS ONE*, **7**(2):
827 e31497.
828 Fedorov A, Beichel R, Kalpathy-Cramer J, et al. 2012. 3D Slicer as an image computing
829 platform for the Quantitative Imaging Network. *Magn Reson Imaging*, **30**(9): 1323-1341.
830 Feng Z, Li X, Luo Y, et al. 2025. A mouse brain stereotaxic topographic atlas with isotropic 1-
831 mum resolution. *Nature*, **645**(8080): 448-456.
832 Ferraris S, Van Der Merwe J, Van Der Veeken L, et al. 2018. A magnetic resonance multi-atlas
833 for the neonatal rabbit brain. *NeuroImage*, **179**: 187-198.
834 Goerzen D, Fowler C, Devenyi GA, et al. 2020. An MRI-Derived Neuroanatomical Atlas of the
835 Fischer 344 Rat Brain. *Sci Rep*, **10**(1): 6952.
836 Gorgolewski KJ, Auer T, Calhoun VD, et al. 2016. The brain imaging data structure, a format
837 for organizing and describing outputs of neuroimaging experiments. *Scientific Data*, **3**(1):
838 160044.
839 Han Y, Zhou J, Zhang R, et al. 2024. Genome-edited rabbits: Unleashing the potential of a
840 promising experimental animal model across diverse diseases. *Zool Res*, **45**(2): 253-262.
841 Hayrapetyan NK & Badalyan IA. 2023. Correction by Antioxidants of Oxidative Activity in an
842 Experimental Model of Parkinson's Disease. *Proceedings of the YSU B: Chemical and*
843 *Biological Sciences*, **57**(3 (262)): 282-291.
844 Hikishima K, Komaki Y, Seki F, et al. 2017. In vivo microscopic voxel-based morphometry with
845 a brain template to characterize strain-specific structures in the mouse brain. *Sci Rep*, **7**(1): 85.
846 Isensee F, Jaeger PF, Kohl SaA, et al. 2021. nnU-Net: a self-configuring method for deep
847 learning-based biomedical image segmentation. *Nat Methods*, **18**(2): 203-211.

Uncorrected proof

Jin P, Pan Y, Pan Z, et al. 2018. Alzheimer-like brain metabolic and structural features in cholesterol-fed rabbit detected by magnetic resonance imaging. *Lipids Health Dis*, **17**(1): 61.

Jung B, Taylor PA, Seidlitz J, et al. 2021. A comprehensive macaque fMRI pipeline and hierarchical atlas. *NeuroImage*, **235**: 117997.

Kim Y, Lee YB, Bae SK, et al. 2021. Development of a photochemical thrombosis investigation system to obtain a rabbit ischemic stroke model. *Sci Rep*, **11**(1): 5787.

Kleven H, Bjerke IE, Clasca F, et al. 2023. Waxholm Space atlas of the rat brain: a 3D atlas supporting data analysis and integration. *Nat Methods*, **20**(11): 1822-1829.

Leao AH, Sarmento-Silva AJ, Santos JR, et al. 2015. Molecular, Neurochemical, and Behavioral Hallmarks of Reserpine as a Model for Parkinson's Disease: New Perspectives to a Long-Standing Model. *Brain Pathol*, **25**(4): 377-390.

Lee BC, Lin MK, Fu Y, et al. 2021. Multimodal cross-registration and quantification of metric distortions in marmoset whole brain histology using diffeomorphic mappings. *J Comp Neurol*, **529**(2): 281-295.

Liu C, Ye FQ, Yen CC-C, et al. 2018. A digital 3D atlas of the marmoset brain based on multi-modal MRI. *NeuroImage*, **169**: 106-116.

Liu CR, Yen CCC, Szczupak D, et al. 2021. Marmoset Brain Mapping V3: Population multi-modal standard volumetric and surface-based templates. *NeuroImage*, **226**: 117620.

Lv Q, Yan M, Shen X, et al. 2021. Normative Analysis of Individual Brain Differences Based on a Population MRI-Based Atlas of Cynomolgus Macaques. *Cereb Cortex*, **31**(1): 341-355.

Ma Y, Smith D, Hof PR, et al. 2008. In Vivo 3D Digital Atlas Database of the Adult C57BL/6J Mouse Brain by Magnetic Resonance Microscopy. *Front Neuroanat*, **2**: 1.

uncorrected proof

Mackenzie-Graham AJ, Lee EF, Dinov ID, et al. 2007. Multimodal, multidimensional models of mouse brain. *Epilepsia*, **48 Suppl 4**(Suppl 4): 75-81.

Manger P. 2008. Is 21st Century Neuroscience too Focussed on the Rat/Mouse Model of Brain Function and Dysfunction? *Frontiers in Neuroanatomy*, **2**: 5.

Manjon JV, Coupe P, Marti-Bonmati L, et al. 2010. Adaptive non-local means denoising of MR images with spatially varying noise levels. *J Magn Reson Imaging*, **31**(1): 192-203.

Mansour H, Azrak R, Cook JJ, et al. 2025. The Duke Mouse Brain Atlas: MRI and light sheet microscopy stereotaxic atlas of the mouse brain. *Sci Adv*, **11**(18): eadq8089.

Marbacher S, Milavec H, Neuschmelting V, et al. 2011. Outer skull landmark-based coordinates for measurement of cerebral blood flow and intracranial pressure in rabbits. *Journal of Neuroscience Methods*, **201**(2): 322-326.

Marques JP, Khabipova D, Gruetter R. 2017. Studying cyto and myeloarchitecture of the human cortex at ultra-high field with quantitative imaging: R(1), R(2)(*) and magnetic susceptibility. *NeuroImage*, **147**: 152-163.

Martinez-Tazo P, Santos A, Selim MK, et al. 2024. Sex matters: The MouseX DW-ALLEN Atlas for mice diffusion-weighted MR imaging. *NeuroImage*, **292**: 120573.

Mullhaupt D, Augsburger H, Schwarz A, et al. 2015. Magnetic resonance imaging anatomy of the rabbit brain at 3 T. *Acta Vet Scand*, **57**(1): 47.

Muñoz-Moreno E, Arbat-Plana A, Batalle D, et al. 2013. A Magnetic Resonance Image Based Atlas of the Rabbit Brain for Automatic Parcellation. *PLOS ONE*, **8**(7): e67418.

Narayan SK, Grace Cherian S, Babu Phaniti P, et al. 2021. Preclinical animal studies in ischemic stroke: Challenges and some solutions. *Animal Model Exp Med*, **4**(2): 104-115.

Uncorrected proof

892 Nie B, Wu D, Liang S, et al. 2019. A stereotaxic MRI template set of mouse brain with fine sub-
893 anatomical delineations: Application to MEMRI studies of 5XFAD mice. *Magn Reson Imaging*,
894 **57**: 83-94.
895 Nitzsche B, Boltze J, Ludewig E, et al. 2019. A stereotaxic breed-averaged, symmetric T2w
896 canine brain atlas including detailed morphological and volumetrical data sets. *NeuroImage*,
897 **187**: 93-103.
898 Nitzsche B, Frey S, Collins LD, et al. 2015. A stereotaxic, population-averaged T1w ovine brain
899 atlas including cerebral morphology and tissue volumes. *Front Neuroanat*, **9**: 69.
900 Ouyang F, Chen X, Liang J, et al. 2022. Population-Average Brain Templates and Application
901 to Automated Voxel-Wise Analysis Pipelines for Cynomolgus Macaque. *Neuroinformatics*,
902 **20**(3): 613-626.
903 Plum F. 2004. Atlas of the rabbit brain and spinal cord. By J. W. Shek, G. Y. Wen, and H. M.
904 Wisniewski New York, Karger, 1986 139 pp, illustrated, $151.50. *Annals of Neurology*, **22**(1):
905 100-100.
906 Prior MJW, Bast T, Mcgarrity S, et al. 2021. Ratlas-LH: An MRI template of the Lister hooded
907 rat brain with stereotaxic coordinates for neurosurgical implantations. *Brain Neurosci Adv*, **5**:
908 23982128211036332.
909 Ren BX, Huen I, Wu ZJ, et al. 2021. Early postnatal irradiation-induced age-dependent changes
910 in adult mouse brain: MRI based characterization. *BMC Neurosci*, **22**(1): 28.
911 Rozema NB, Procissi D, Bertolino N, et al. 2020. Abeta oligomer induced cognitive impairment
912 and evaluation of ACU193-MNS-based MRI in rabbit. *Alzheimers Dement (N Y)*, **6**(1): e12087.
913 Sajja BR, Bade AN, Zhou B, et al. 2016. Generation and Disease Model Relevance of a

uncorrected proof

914 Manganese Enhanced Magnetic Resonance Imaging-Based NOD/scid-IL-2Rgammac(null)
915 Mouse Brain Atlas. *J Neuroimmune Pharmacol*, **11**(1): 133-141.
916 Sawyer CH, Everett JW, Green JD. 1954. The rabbit diencephalon in stereotaxic coordinates.
917 *J Comp Neurol*, **101**(3): 801-824.
918 Schroeder MP, Weiss C, Procissi D, et al. 2016. Intrinsic connectivity of neural networks in the
919 awake rabbit. *NeuroImage*, **129**: 260-267.
920 Seo J, Lee JW, Cho J, et al. 2022. A rabbit model for embolic infarct potentials of injectables
921 using ultrasound-guided carotid artery puncture. *Sci Rep*, **12**(1): 19269.
922 Seyhan AA. 2019. Lost in translation: the valley of death across preclinical and clinical divide –
923 identification of problems and overcoming obstacles. *Translational Medicine Communications*,
924 **4**(1): 18.
925 Stewart AW, Robinson SD, O'brien K, et al. 2022. QSMxT: Robust masking and artifact
926 reduction for quantitative susceptibility mapping. *Magn Reson Med*, **87**(3): 1289-1300.
927 Tian X, Chen Y, Majka P, et al. 2022. An integrated resource for functional and structural
928 connectivity of the marmoset brain. *NATURE COMMUNICATIONS*, **13**(1): 7416.
929 Tustison NJ, Avants BB, Cook PA, et al. 2010. N4ITK: improved N3 bias correction. *IEEE Trans*
930 *Med Imaging*, **29**(6): 1310-1320.
931 Wang Q, Ding SL, Li Y, et al. 2020. The Allen Mouse Brain Common Coordinate Framework:
932 A 3D Reference Atlas. *Cell*, **181**(4): 936-953 e920.
933 Weiskopf N, Edwards LJ, Helms G, et al. 2021. Quantitative magnetic resonance imaging of
934 brain anatomy and in vivo histology. *Nature Reviews Physics*, **3**(8): 570-588.
935 Weiss C, Bertolino N, Procissi D, et al. 2022a. Diet-induced Alzheimer's-like syndrome in the

uncorrected proof

936 rabbit. *Alzheimers Dement (N Y)*, **8**(1): e12241.

937 Weiss C, Bertolino N, Procissi D, et al. 2022b. Brain activity studied with magnetic resonance

938 imaging in awake rabbits. *Front Neuroimaging*, **1**: 965529.

939 Weiss C, Procissi D, Power JM, et al. 2018. The rabbit as a behavioral model system for

940 magnetic resonance imaging. *J Neurosci Methods*, **300**: 196-205.

941 Wharton S, Schafer A, Bowtell R. 2010. Susceptibility mapping in the human brain using

942 threshold-based k-space division. *Magn Reson Med*, **63**(5): 1292-1304.

943 Wu B, Li W, Guidon A, et al. 2012. Whole brain susceptibility mapping using compressed

944 sensing. *Magn Reson Med*, **67**(1): 137-147.

945 Xie R, Han F, Yu Q, et al. 2025. A movable long-term implantable soft microfibre for dynamic

946 bioelectronics. *Nature*, **645**(8081): 648-655.

947 Yang JP, Liu HJ, Liu RC. 2009. A modified rabbit model of stroke: evaluation using clinical MRI

948 scanner. *Neurol Res*, **31**(10): 1092-1096.

949 Yang Y, Zhang Q, Ren J, et al. 2022. In vivo symmetric multi-contrast MRI brain templates and

950 atlas for spontaneously hypertensive rats. *Brain Struct Funct*, **227**(5): 1789-1801.

951 Yoshida A, Ye FQ, Yu DK, et al. 2021. Visualization of iron-rich subcortical structures in non-

952 human primates in vivo by quantitative susceptibility mapping at 3T MRI. *NeuroImage*, **241**:

953 118429.

954 Zhang Z, Song Y, Lai L, et al. 2022. Genome-edited rabbit, a prospective alternative model for

955 neurological diseases. *Ageing and Neurodegenerative Diseases*, **2**(3): 16.

956 Zhu X, Yan H, Zhan Y, et al. 2023. An anatomical and connectivity atlas of the marmoset

957 cerebellum. *Cell Reports*, **42**(5): 112480.

uncorrected proof

Zhuang J, Stoelzel CR, Bereshpolova Y, et al. 2013. Layer 4 in primary visual cortex of the awake rabbit: contrasting properties of simple cells and putative feedforward inhibitory interneurons. *J Neurosci*, **33**(28): 11372-11389.

Tables and figures

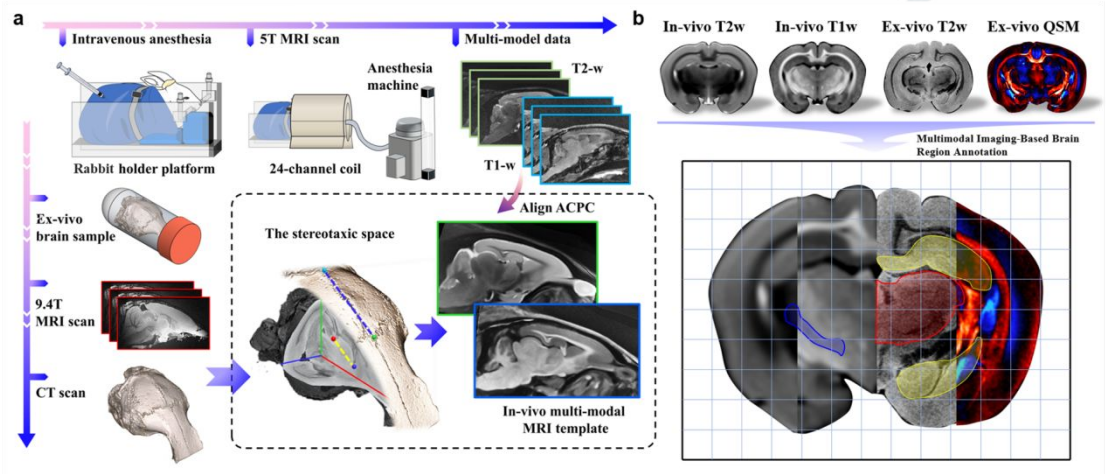


Figure 1 Construction of the RBT multimodal MRI stereotaxic atlas. a, Data acquisition protocols for high-resolution in vivo MRI, ex vivo ultra-high-field MRI (9.4T), and ex vivo Micro-CT. A unified coordinate system incorporating cranial anatomical benchmarks was established using osseous landmarks (Bregma, Lambda) from ex vivo CT and concurrently acquired ex vivo T2w images. Subsequently, a population-representative multimodal in vivo brain template was constructed by mapping all in vivo T1w/T2w data into this standardized space. b, Refined neuroanatomical delineation and annotation. By integrating macroscopic morphology from in vivo imaging, microscopic anatomical details from ex vivo high-resolution T2w imaging, and magnetic susceptibility contrast from QSM, the cortex, white matter, and subcortical nuclei were identified, resulting in a comprehensive anatomical atlas covering the entire brain.

uncorrected

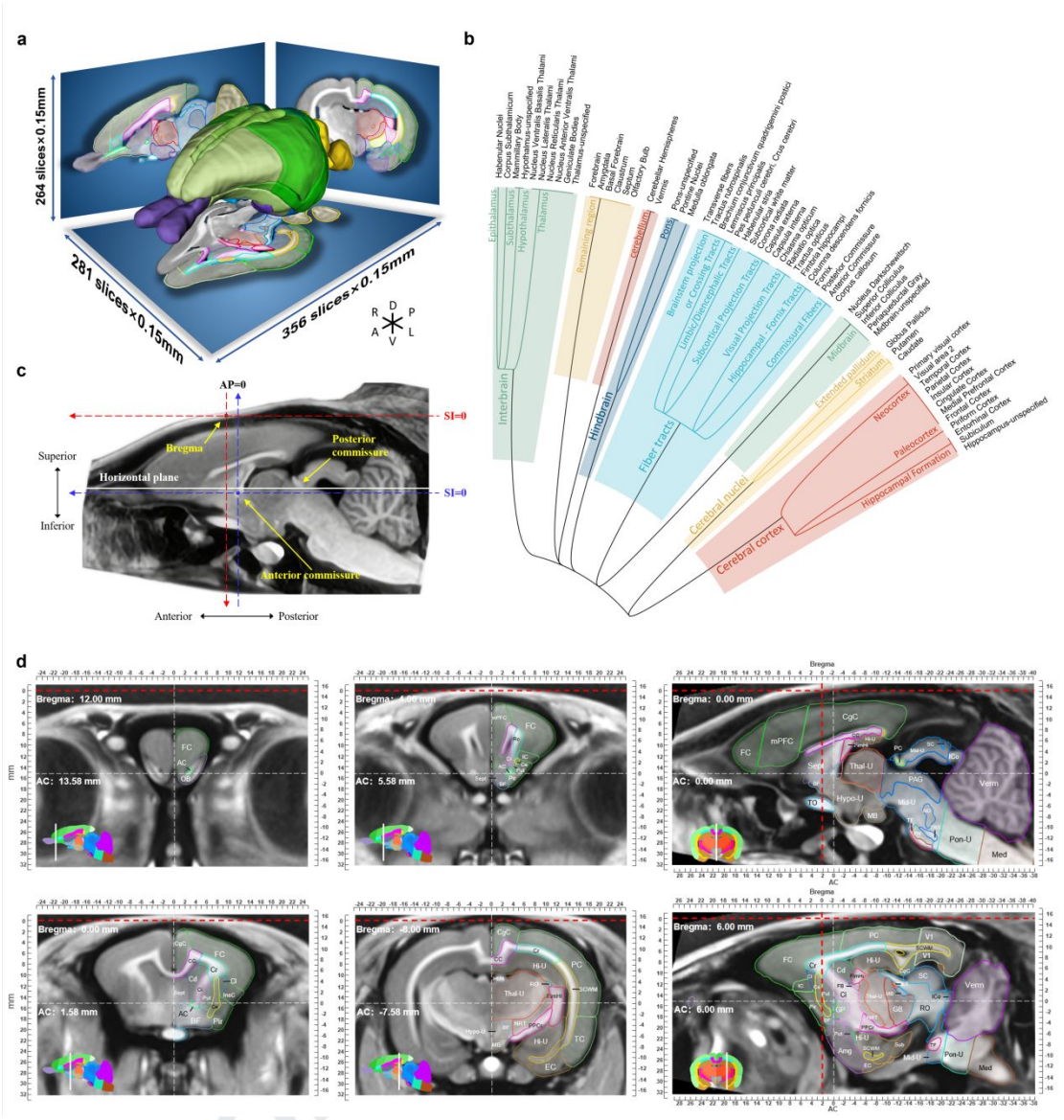


Figure 2 RBT stereotaxic atlas and hierarchical organization. a, 3D representation of the RBT atlas. The 3D framework constructed from the population-averaged template is presented. Whole-brain morphology is displayed via orthogonal sections (coronal, sagittal, and horizontal), with parcellation boundaries delineated by color contours. b, Hierarchical architecture of the atlas. Gray matter is partitioned into four categories based on spatial evolution: interbrain, hindbrain, cerebral nuclei, and cerebral cortex; white matter is subdivided according to functional circuit attributes. c, Stereotaxic dual-coordinate reference system. Integration of the primary skull-based Bregma–Lambda stereotaxic system (red lines) with the internal AC–PC coordinate system (blue lines) in the sagittal plane of the T1w template, displaying the anterior-posterior (Y-axis) and dorsal (Z-axis, superior) axes. d, Coronal parcellation in stereotaxic space. Spatial distribution of the 107 manually segmented brain regions within the integrated dual-coordinate framework, with the primary Bregma–Lambda stereotaxic system indicated by red lines. Coordinate ticks are provided to facilitate precise anatomical localization and stereotaxic targeting.

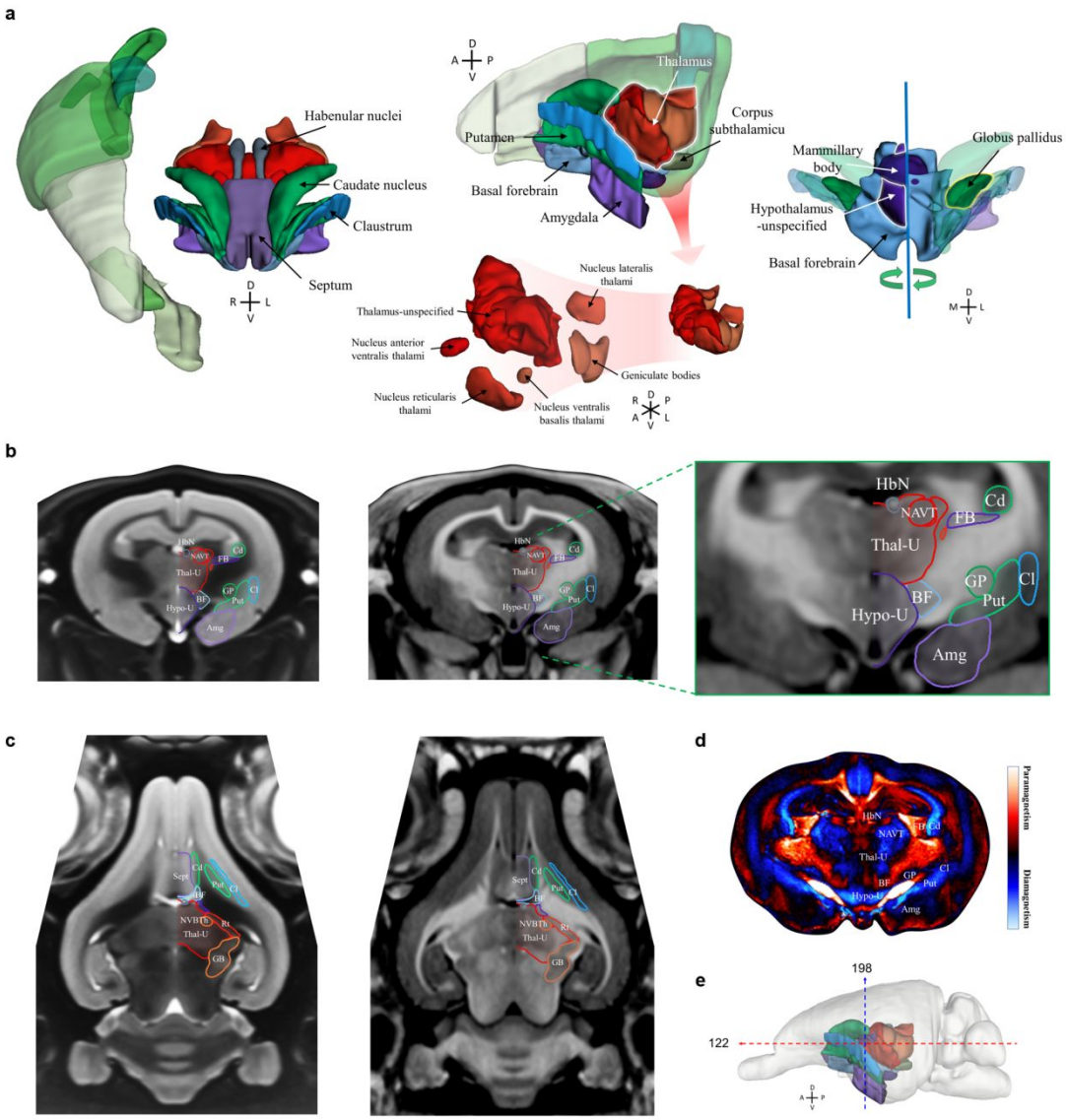


Figure 3 3D reconstruction and spatial distribution of subcortical nuclei. a, 3D spatial distribution and topological structure of rabbit brain nuclei. The left panel presents the anterior aspect of the nuclear structures; the middle view displays the lateral aspect with a 3D disassembly of the thalamic complex to reveal internal architecture; the right panel shows the topological arrangement of subcortical nuclei along the anterior-posterior axis. b, c, Anatomical boundaries of nuclei under multimodal imaging. The anatomical morphology of subcortical nuclei is displayed in coronal (b) and horizontal (c) planes. Boundary characteristics under varying contrasts are presented through multimodal image comparison. d, Corresponding locations of representative slices in QSM. The anatomical accuracy of subcortical nuclei (e.g., thalamus and striatum) is verified at the voxel level leveraging the high tissue contrast provided by QSM. e, Spatial localization of anatomical slices. Using the 3D whole-brain model as a reference, the anatomical positions of the aforementioned slices within the standardized coordinate system are demarcated.

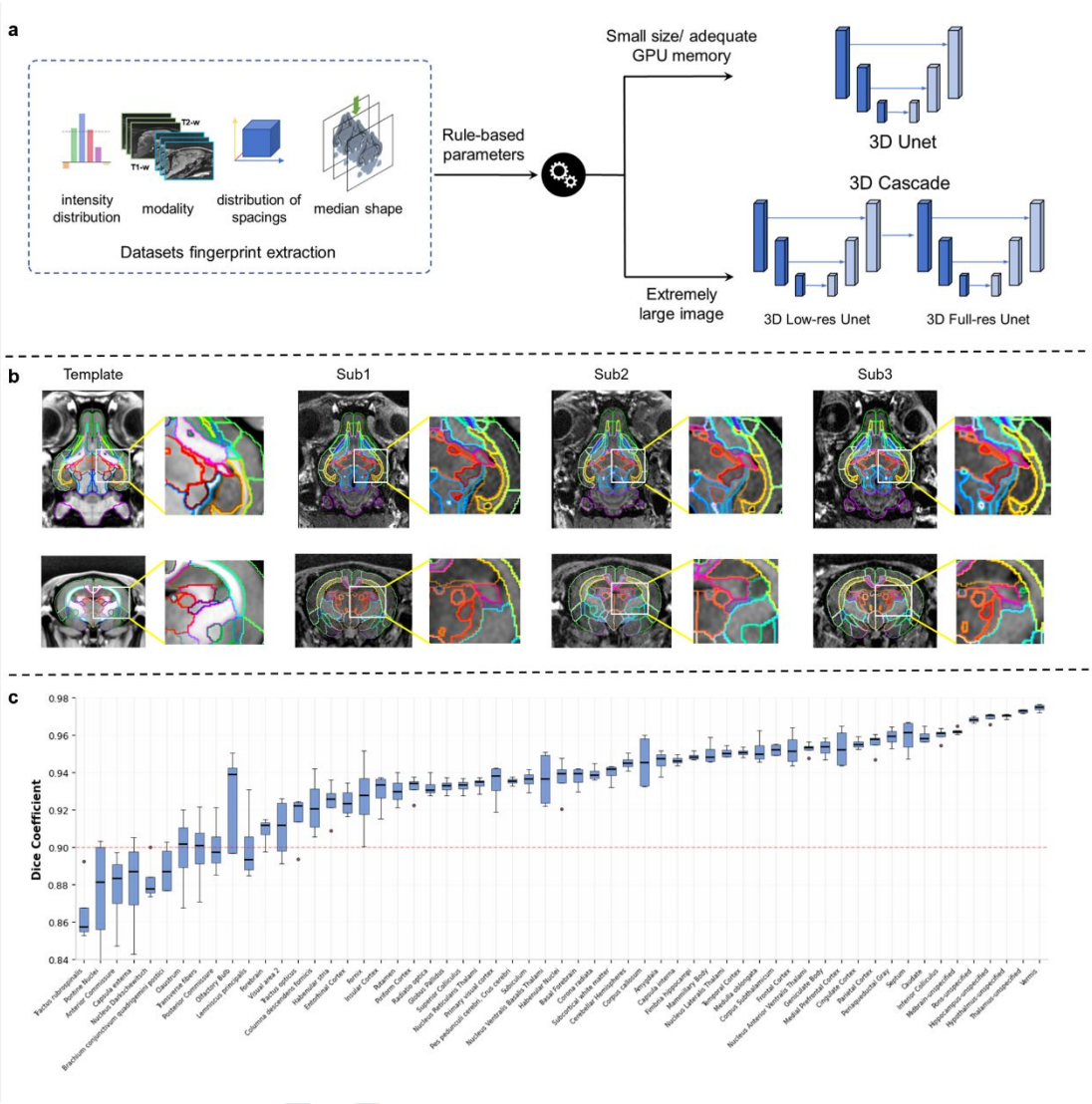


Figure 4 Deep learning-based framework and evaluation for RBT automated segmentation. a, nnU-Net framework: key parameters, including intensity distribution, modalities, and voxel spacing, are extracted via the "dataset fingerprint" module, facilitating the automated selection between 3D U-Net and 3D cascade U-Net architectures. b, Visualization of segmentation results: automated segmentation outcomes are compared against the template across coronal and axial slices from three representative individuals to demonstrate boundary consistency. c, Dice Similarity Coefficient (DSC) calculation: segmentation accuracy is quantified by calculating the DSC for each brain region relative to the template-based ground truth.

Uncorrected Proof

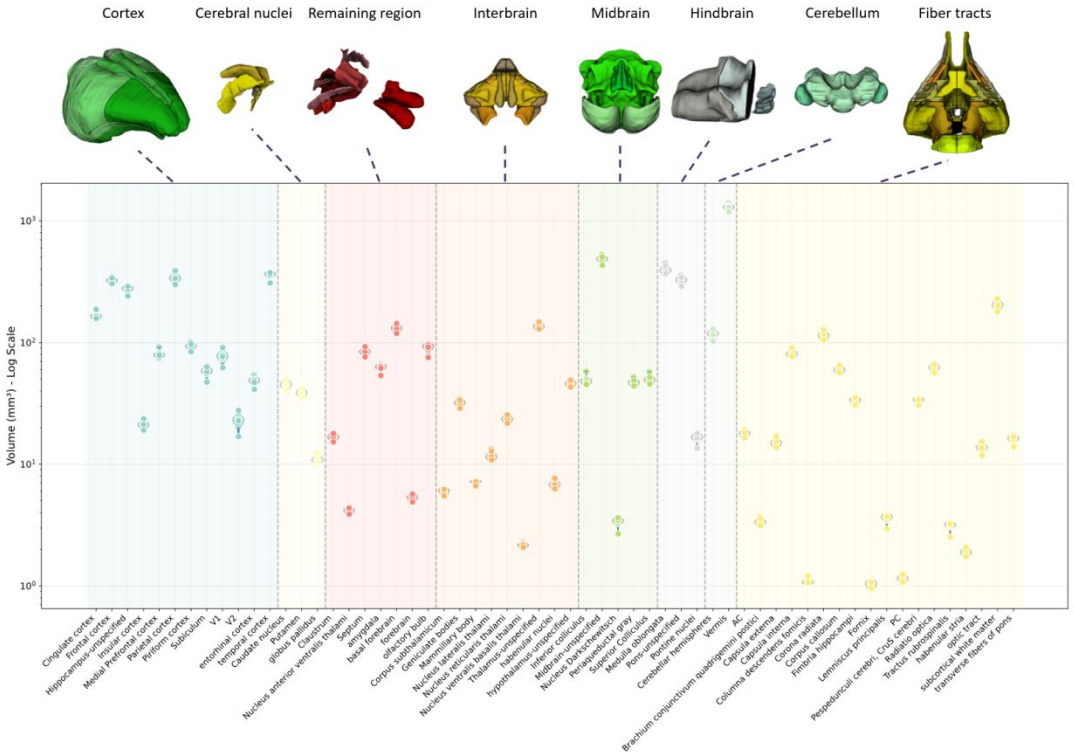


Figure 5 Volume distribution of 107 brain regions in the rabbit atlas. Based on a hierarchical system, regions were grouped into eight major anatomical divisions. After combining bilateral structures, absolute volumes (mm^3) were log-transformed. The plots illustrate the distribution across categories, reflecting the morphological consistency across subjects.

uncorrected

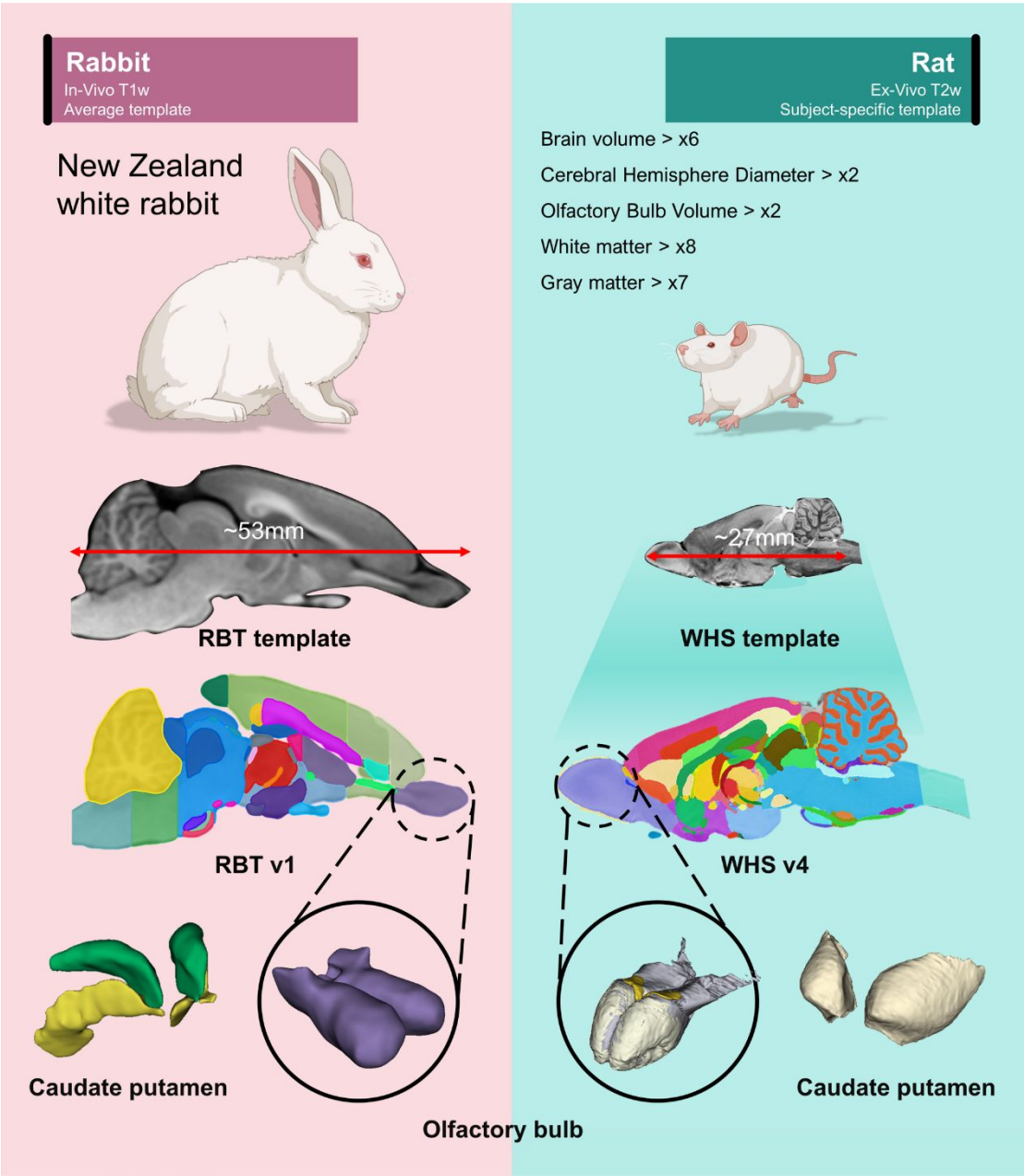


Figure 5 Cross-species morphological comparison of whole-brain anatomy between rabbit and rat. The rabbit brain exhibits approximately 6-fold larger total volume, 2-fold greater cerebral hemisphere diameter, and 2-fold larger olfactory bulb volume compared to the rat. White matter volume is ～8 times greater and gray matter volume ～7 times greater in the rabbit. Additionally, the rabbit striatum is fully differentiated, in contrast to the less distinct striatal organization observed in the rat. Rat brain data sourced from the Waxholm Space atlas.